

Plasma Characterization Using Ultraviolet Thomson Scattering from Ion-Acoustic and Electron Plasma Waves

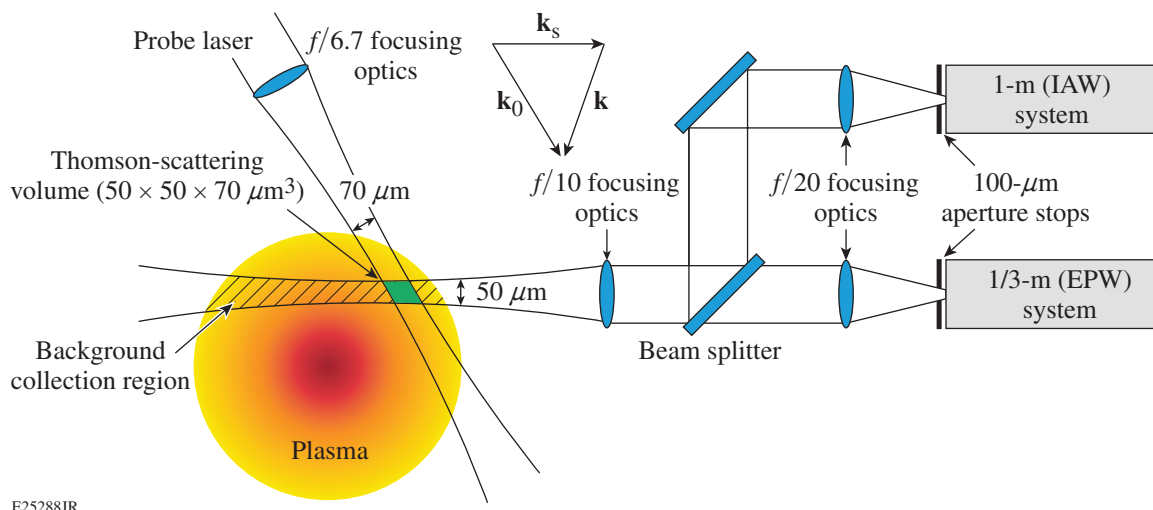
Introduction

Optical Thomson scattering from collective plasma oscillations is a standard technique for diagnosing underdense plasma conditions in high-energy-density-physics experiments.¹ Thomson scattering is used to make spatially² and temporally resolved^{3–5} measurements of the electron temperature (T_e), ion temperature (T_i), electron density (n_e), fluid velocity (\mathbf{u}), heat flux, ionization state (Z), and ion species fractions (for a multiple ion species plasma). Thomson scattering is used here to diagnose a number of plasma-wave instabilities including stimulated Brillouin scattering,^{6–8} stimulated Raman scattering,⁹ two-ion decay,¹⁰ and two-plasmon decay.^{11,12}

Thomson-scattering diagnostics take a local measurement of the plasma conditions averaged over a small volume (typically $\sim 50 \mu\text{m}^3$). The Thomson-scattering volume is created by overlapping the waist of the probe laser with an aperture stop within the collection system [typically a pinhole at the spectrometer's entrance (see Fig. 147.16)]. Light scattered from

the Thomson-scattering volume is collected by a telescope and transported to a spectrometer/streak-camera pair to obtain spectral and temporal resolution.²

By conserving momentum ($\mathbf{k}_0 = \mathbf{k}_s + \mathbf{k}$), Thomson-scattering probes the plasma waves with wavelengths $\lambda = 2\pi/|\mathbf{k}|$ (\mathbf{k}_0 , \mathbf{k}_s , and \mathbf{k} are the wave vectors of the probe beam, scattered light, and plasma wave, respectively). The normal modes of the plasma are observed in the Thomson-scattering spectra when probing the appropriate wavelengths, and the measured frequencies of these normal modes provide a powerful diagnostic of the plasma conditions. This collective Thomson-scattering regime is typically characterized by comparing the probed wavelength to the Debye length [$\lambda_{De} \equiv v_{te}/\omega_{pe}$, where $v_{te} = \sqrt{T_e/m_e}$ is the electron thermal velocity, $\omega_{pe} = \sqrt{4\pi e^2 n_e/m_e}$ is the plasma frequency in centimeter-gram-second (cgs) units, and m_e is the electron mass]. When $k\lambda_{De} < 1$, electron plasma wave (EPW) features are present in the spectrum; when $k\lambda_{De} < \sqrt{ZT_e/T_i}$, ion-acoustic features are observed.



E25288JR

Figure 147.16

Thomson-scattering diagnostic configuration on OMEGA. Note that the schematic shows transmissive optics but the actual focusing/collection optics were reflective. IAW: ion-acoustic wave; EPW: electron plasma wave.

In practice, the complete shape of the Thomson-scattering spectrum is used to determine the plasma conditions by integrating the differential Thomson-scattered power per unit frequency per unit solid angle per unit volume over the Thomson-scattering volume and the solid angle of the collection optic:¹

$$\frac{\partial^3 P_s}{\partial \omega \partial \Omega \partial V} = \frac{I_0 n_e r_0^2}{2\pi} \left| \hat{k}_s \times (\hat{k}_s \times \hat{E}_0) \right| \left(1 + \frac{2\omega}{\omega_0} \right) S(k, \omega), \quad (1)$$

where I_0 is the incident probe-beam intensity, $r_0 = e^2/m_e c^2$ is the classical electron radius, \hat{E}_0 is the polarization direction of the probe beam, and $\omega(\omega_0)$ is the frequency of the plasma wave (probe beam). The frequency of the scattered light is given by the matching condition

$$\omega_s = \omega_0 - \omega, \quad (2)$$

where $\omega \in \mathbb{R}$ and waves with negative frequency propagate antiparallel to \mathbf{k} .

The dynamic form factor (neglecting collisions and in the absence of applied magnetic fields) is derived from the linearized Vlasov equation (and Poisson's equation),

$$S(\mathbf{k}, \omega) = \frac{(k\lambda_{De})^2}{\pi\omega} \left[\left| 1 - \frac{\chi_e}{\varepsilon} \right|^2 \text{Im}\{\chi_e\} + \sum_j \frac{Z_j^2 n_{ij} T_{ij}}{n_i T_e} \left| \frac{\chi_e}{\varepsilon} \right|^2 \text{Im}\{\chi_{i,j}\} \right], \quad (3)$$

where the sum is over ion species, $n_{i,j}(T_{i,j})$ is the number density (temperature) of the j^{th} ion species, $n_i = \sum_j Z_j n_{i,j}$, and $\varepsilon \equiv 1 + \chi_e + \sum_j \chi_{i,j}$ is the plasma dielectric function. The electron (χ_e) and ion (χ_i) susceptibilities are

$$\chi_s(\mathbf{k}, \omega) = \frac{4\pi q_s^2 n_{s0}}{m_s k^2} \int_{-\infty}^{\infty} d\mathbf{v} \frac{\mathbf{k} \cdot \partial f_{s0} / \partial \mathbf{v}}{\omega - \mathbf{k} \cdot \mathbf{v} - i\gamma}, \quad (4)$$

where n_{s0} and f_{s0} are the unperturbed number density and velocity distribution, respectively.

The dominant modes observed in collective Thomson-scattering experiments are given by the real part of the roots of $\varepsilon(\mathbf{k}, \omega) = 0$. The difference in frequency between the scattered light and probe beam in the lab frame is determined by

substituting the lab frame probe ($\omega'_0 + \mathbf{k}_0 \cdot \mathbf{u}$) and scattered-light ($\omega'_s = \omega_s + \mathbf{k}_s \cdot \mathbf{u}$) frequencies and the plasma-wave frequency into Eq. (2), which, for scattering from ion-acoustic waves, gives

$$\Delta\omega_{\pm} = (\omega'_s - \omega'_0) = \pm k c_s - \mathbf{k} \cdot \mathbf{u}, \quad (5)$$

and from EPW's

$$\Delta\omega_{\pm} = (\omega'_s - \omega'_0) = \pm \sqrt{\omega_{pe}^2 + 3k^2 v_{te}^2} - \mathbf{k} \cdot \mathbf{u}, \quad (6)$$

where $\Delta\omega_{\pm}$ corresponds to the frequency shift in the blue- and red-shifted light and $c_s = \sqrt{(ZT_e + 3T_i)/m_i}$ is the sound speed (m_i is the ion mass).

Equation (5) shows that the frequencies of the two ion-acoustic wave (IAW) spectral peaks are given by the sound speed, fluid velocity, and plasma-wave vector. The frequency of the peaks in the EPW spectrum is dominated by the electron density because the contribution to the frequency shift related to the ω_{pe}^2 term in Eq. (6) is typically much larger than the contribution from the other terms. To obtain further information from Thomson-scattering spectra, synthetic power spectra generated using the kinetic description [Eq. (1)] are directly compared to measured spectra. In theory, arbitrary moments of the unperturbed velocity distributions (or their projections along \mathbf{k}) can be inferred by fitting Eq. (1) to measured spectra, but experimental uncertainties and degeneracy between parameter variations limit practical measurements to the fourth moment (heat flux) and require the shape of the unperturbed velocity distribution (f_{s0}) to be assumed (e.g., Maxwellian or Maxwellian with polynomial corrections).^{13,14}

A common challenge in determining accurate plasma conditions from Thomson-scattering spectra is that measured spectra have broader peaks than calculated spectra. This has been attributed to ion-ion collisions,^{13,15} plasma gradients, and probing a range of wave vectors.¹⁶ As a first-order approximation, these effects can be accounted for by convolving the calculated spectra with a Gaussian response function. A physically consistent model is required, however, to measure parameters that depend on the detailed shape and not just the frequency of the spectral peaks.

The impact of gradients on Thomson-scattering measurements can be approximated by comparing the derivatives of Eqs. (5) and (6) to the linear Landau-damping rates. Gradient effects can be neglected when the broadening of the spectral peaks related to gradients is much less than the broadening

caused by damping. In the weak damping limit, the damping rate is given by the imaginary part of the dielectric function divided by the spectral derivative of its real part evaluated at the normal mode frequency $[\omega_i = -\epsilon_i / (\partial\epsilon_r / \partial\omega)]$ (Ref. 17). Simplifying to 1-D, the dominant term in broadening of the spectral peaks caused by spatial gradients in Eq. (5) is typically the fluid velocity gradient $\delta\omega_{\pm} = \delta x k \partial u / \partial x$, and variations in the probed wave vector give $\delta\omega_{\pm} = \delta k (\pm c_s - u)$. Wave-vector variations are typically negligible in Eq. (6) and the dominant spatial term is $\delta\omega_{\pm} = \delta x \omega_{pe} / L_n$, where L_n is the density scale length.

Some of the physical effects that should be included when fitting measured Thomson-scattering spectra to calculated spectra are presented in this article. The following sections (1) present experimentally measured Thomson-scattering spectra from IAW's and EPW's from a series of direct-drive inertial confinement fusion implosions¹⁸ on the OMEGA laser¹⁹ and discuss spectral calibration and background radiation; (2) describe the techniques used to analyze the measured spectra; (3) present the methods used to calculate the plasma gradients and compare the results of fitting Thomson-scattering data with and without accounting for gradient effects; (4) discuss error analysis and present the results of applying these techniques to the measured scattering spectra; and (5) summarize our findings.

Thomson-Scattering Measurements

The Thomson-scattering diagnostic on OMEGA consists of a reflective $f/10$ collection system coupled to two spectrometer/streak-camera pairs.² The $f/6.7$ probe beam ($\lambda_{4\omega} = 263.25$ nm) had a best-focus diameter of ~ 70 μm (Ref. 20). The spectral resolutions of the IAW and EPW systems were 0.05 nm and 0.5 nm, respectively. The scattering volume was $\sim 50 \times 50 \times 70$ μm^3 . The angle between the probe beam and collection optic was 120° .

Figure 147.17 shows IAW and EPW Thomson-scattering spectra taken during 60-beam ($\lambda_{3\omega} = 351$ -nm) implosions on the OMEGA laser with the Thomson-scattering diagnostic configured to probe wave vectors perpendicular to the target normal. The targets were 870- μm -diam, 23- μm -thick spherical CH shells filled with 10 atm of D_2 gas. The laser pulse was a 1.2-ns square pulse preceded by three 100-ps picket pulses with a total energy of 12 kJ. Distributed phase plates²¹ were used on each beam to define 860- μm full width at 95% flattop laser spots using $f/6.7$ lenses.

1. Spectral Sensitivity

The spectral sensitivity of the Thomson-scattering diagnostic was calculated using

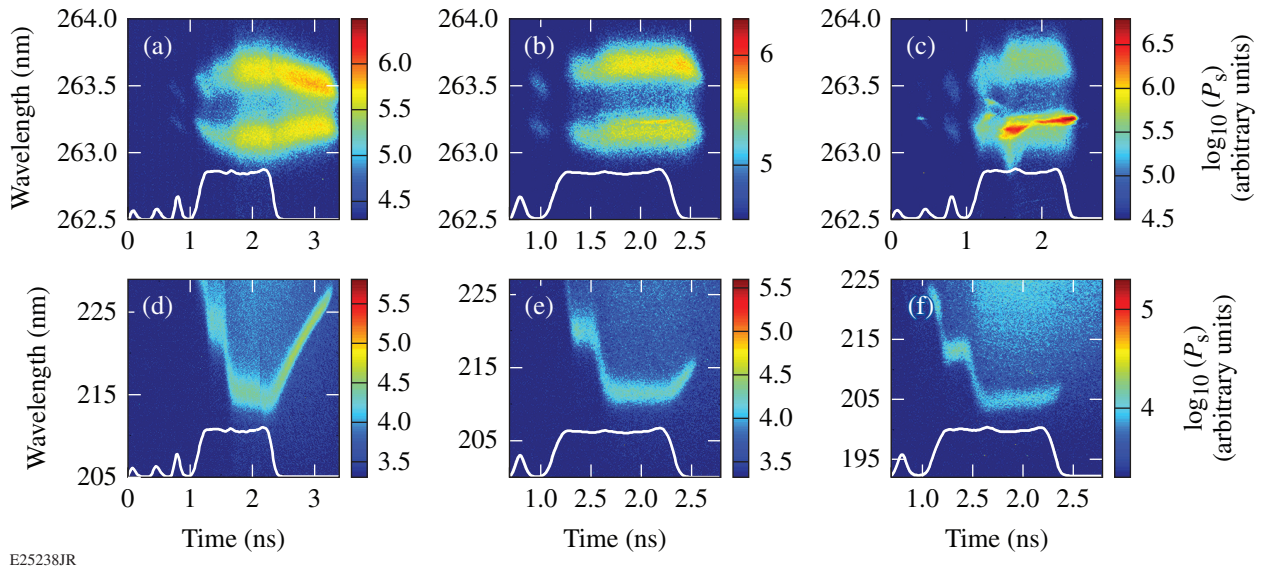
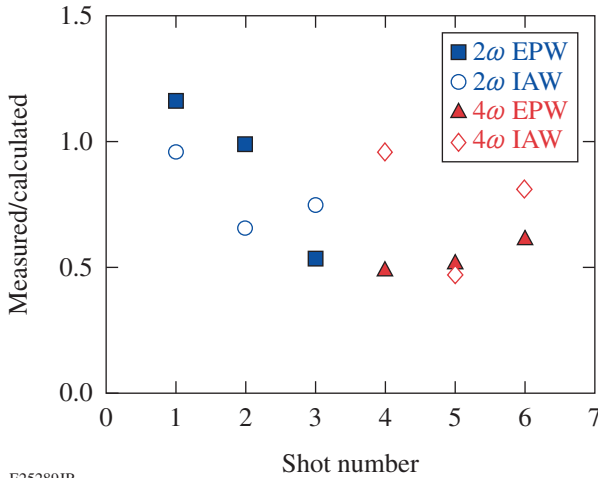


Figure 147.17 Thomson scattering from [(a)–(c)] IAW's and [(d)–(f)] EPW's at [(a),(d)] 400 μm , [(b),(e)] 300 μm , and [(c),(f)] 200 μm from the initial target surface. The drive-laser pulse shape is overlaid. The bright features at ~ 263.2 nm in the IAW spectra correspond to reflected or refracted light from the probe beam.

$$C(\lambda) = \frac{m \cdot k \cdot G \cdot px}{M} \left(\frac{\lambda}{hc} \right) Q(\lambda) T(\lambda) \frac{\text{CCD } e^- \cdot \text{nm}}{\text{pixel} \cdot \text{watt}},$$

the system parameters of which are shown in Table 147.I ($h = 6.62 \times 10^{-27}$ erg · s). The number of charge-coupled-device (CCD) counts per pixel is given by the product of the sensitivity with the power scattered $[C(\lambda) \int d\Omega \int dV \partial^3 P_s / \partial \lambda \partial \Omega \partial V]$, where $\partial P_s / \partial \lambda = (d\omega / d\lambda) \partial P_s / \partial \omega$ integrated over the scattering volume and the solid angle of the collection optics.

Figure 147.18 shows the ratio of measured-to-calculated signals for a variety of Thomson-scattering configurations (planar and spherical targets using 2ω and 4ω probe beams). The predictions are within a factor of 2 of the measured values, which is sufficient for determining appropriate probe energies and filtering when designing experiments. Although the fits shown



E25289JR

Figure 147.18

The ratio of measured-to-calculated peak scattering signals for the IAW and EPW features using 2ω (526.5-nm) and 4ω (263.25-nm) probe beams.

in this article were normalized to minimize χ^2 , it was necessary to account for the spectral sensitivity of the detector when fitting the EPW spectra because the sensitivity varied significantly (factor of 2) over the range of wavelengths included in the fits.

2. Background Radiation

The two primary sources of background radiation are bremsstrahlung and Thomson scattering from beams other than the Thomson probe. The two types of background radiation can be distinguished by noting that self-Thomson scattering of the drive beams occurs only when the drive lasers are on, while bremsstrahlung radiation can persist beyond the end of the laser pulse. The background radiation from Thomson scattering of other beams can be calculated using Eq. (1). The differential bremsstrahlung power in watts per unit wavelength (λ) per unit volume (V) per unit solid angle (Ω) is¹

$$\frac{\partial^3 P_{\text{Br}}}{\partial \lambda \partial \Omega \partial V} = \frac{6.61 \times 10^{-35}}{4\pi} \frac{g Z_{\text{eff}}^2 n_e^2}{\lambda^2 T_e^{1/2}} e^{-0.124/\lambda T_e}, \quad (7)$$

where $Z_{\text{eff}}^2 = \langle Z^2 \rangle / \langle Z \rangle$, n_e is in cm^{-3} , λ is in cm, T_e is in keV, and the Gaunt factor $g \sim 1$.

Because the background radiation comes from the entire conical volume observed by the Thomson-scattering diagnostic, an accurate calculation of the background radiation requires spatially resolved knowledge of the plasma conditions along the entire line of sight of the Thomson-scattering collection system (Fig. 147.16). For all of the analysis in this article, the bremsstrahlung radiation was calculated by ray tracing simulations from the radiation-hydrodynamics code *LILAC*²² from the collection optic back through the plasma while integrating Eq. (7) along the rays. The amount of background radiation observed by the diagnostic as a function of the distance from the image plane in the plasma is approximately constant because the col-

Table 147.I: Calibration parameters for the OMEGA Thomson-scattering diagnostic.

Parameter	Symbol	Value	Units
Optical transmission	$T(\lambda)$	~ 0.01	
Photocathode quantum efficiency	$Q(\lambda)$	~ 0.1	Photoelectron/photon
Spectrometer dispersion	m	0.002 to 0.03	nm/ μm at PC
Sweep rate	k	1.1×10^{-12}	s/ μm at CCD
Streak-tube gain	G	150	CCD electron/photoelectron
Pixel size	px	170	$\mu\text{m}^2/\text{pixel}$
Tube magnification	M	1.3	

PC: photocathode; CCD: charge-coupled device.

lection efficiency of the diagnostic falls off at the same rate as the area of the observed conical cross section increases. For practical estimates, a cylinder with the diameter of the optical aperture stop at the plasma image plane and a length sufficient to include the entire plasma along the view of the collection system is a reasonable background-collection volume.

Analysis

The plasma parameters in the Thomson-scattering data shown in Fig. 147.17 were inferred by minimizing $\chi^2 = \int d\lambda [a_s P_s(\lambda) + a_B P_B(\lambda) - P_M(\lambda)]^2$ for a series of spectral lineouts at different times (P_s , P_B , and P_M are the calculated Thomson-scattered power, the calculated background power, and the measured power, respectively; a_s and a_B are normalization coefficients). Distinct normalization coefficients were used for the Thomson-scattered and background radiation because their relative intensities are sensitive to optical alignment. The coefficients were determined by differentiating χ^2 with respect to a_s and a_B and solving the resulting system of equations:

$$a_s \equiv \frac{\left(\int d\lambda P_M P_s\right)\left(\int d\lambda P_B^2\right) - \left(\int d\lambda P_M P_B\right)\left(\int d\lambda P_s P_B\right)}{\left(\int d\lambda P_s^2\right)\left(\int d\lambda P_B^2\right) - \left(\int d\lambda P_s P_B\right)^2},$$

$$a_B \equiv \frac{\int d\lambda P_B^2 (P_M - a_s P_s)}{\int d\lambda P_B^2}.$$

Figure 147.19 shows spectra (averaged over 50 ps) from Figs. 147.17(a) and 147.17(d) taken at 2.8 ns. The spectra are compared to the best-fit spectra calculated with and without

gradients. The IAW fit calculated without gradients is not even qualitatively similar to the measurement, while the EPW spectrum is reasonably well reproduced except in the wings of the spectral peak. The electron temperatures inferred independently from the EPW (1.15-keV) and IAW (0.77-keV) spectra were not self-consistent, and the ion temperature inferred from the IAW (1.62-keV) spectrum was unphysically high for the experimental configuration.

Gradients

1. Plasma Gradients

When gradients are present, the observed scattered light is a superposition of scattering from the various plasma conditions present within the scattering volume (spatially and temporally). The effects of gradients can be included in calculated spectra by taking a weighted sum of spectra calculated at the various plasma conditions.

The typical plasma parameters that are required to account for gradients within the Thomson-scattering volume are the spatial and temporal derivatives of the fluid velocity and electron density. Two methods of approximating the derivatives are ray-tracing hydrodynamic simulations or using mass and momentum conservation to calculate the gradients iteratively using measured spectra.

The fits shown in Fig. 147.19, where gradients were included, are significantly better than those without gradients (without introducing any additional degrees of freedom). Table 147.II compares plasma parameters inferred from the fits with and without gradients and the results of *LILAC* simulations. When

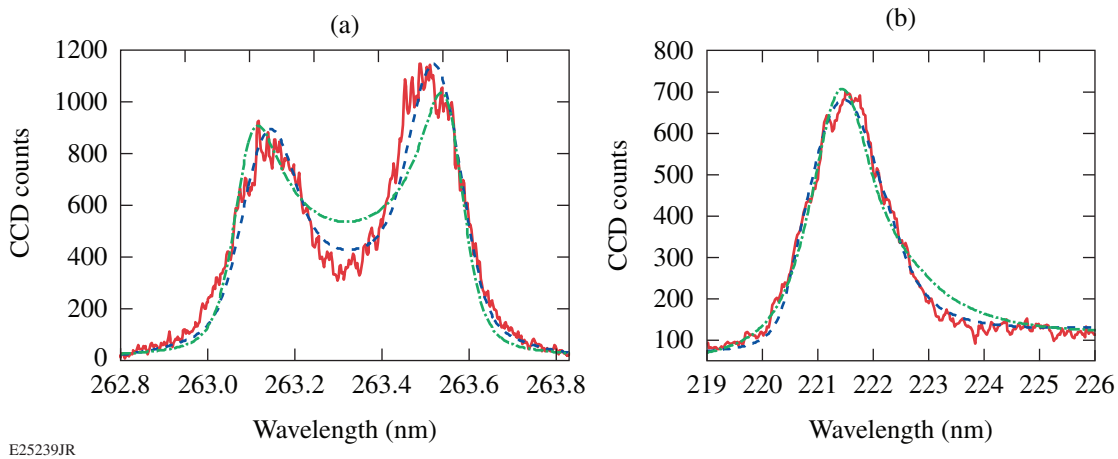


Figure 147.19

Thomson-scattering spectral lineouts at 2.8 ns (400 μm from the target) for scattering from (a) IAW's and (b) EPW's. The solid red curves are the measured spectra, the dashed blue curves are the best fit with gradients included, and the dashed-dotted green curves are the best fit without gradients.

Table 147.II: Comparison of the plasma parameters inferred from the calculated spectra shown in Fig. 147.19. The density is given in 10^{20} cm^{-3} and the temperatures are in keV. The plasma was assumed to be completely ionized. The typical error (see **Error**, p. 131) is $\sim 5\%$ for n_e , $\sim 20\%$ for T_e from the EPW, $\sim 5\%$ for T_e from the IAW, and $\sim 40\%$ for T_i .

	EPW fits		IAW fits	
	n_e	T_e	T_e	T_i
Gradients	4.40	0.93	0.85	0.82
No gradients	4.04	1.15	0.77	1.62
Simulation	4.45	0.78	0.78	0.58

gradients were included in the fits, the electron temperatures inferred from the IAW and EPW spectra were within 10%, and the ion temperature inferred from the IAW spectrum was slightly lower than the electron temperature, consistent with expectations for a laser-ablated plasma a few hundred picoseconds after the end of the laser pulse. The corresponding simulated plasma parameters shown in Table 147.II were also in better agreement with the inferred values when gradients were included in the fits. The electron density inferred from the EPW spectrum and the electron temperature inferred from the IAW spectrum were relatively insensitive to the effects of gradients.

The gradients in plasma parameters used to calculate the spectra in Fig. 147.19 were assumed to be independent and to have a Gaussian distribution of weights. While the gradients in various plasma parameters are not independent in reality, this assumption is valid when the gradient in a single plasma parameter is dominant. The choice of a Gaussian weight distribution was based on the results of ray-trace calculations and is primarily determined by the use of a Gaussian probe beam.

The plasma gradients were calculated by ray tracing density profiles from hydrodynamic simulations. Rays were traced from the probe to the detector and their overlap on a 3-D grid was used to calculate intensity-weighted histograms of the plasma conditions in the Thomson-scattering volume as a function of time. This technique provided a good approximation to the plasma gradients (both temporal and spatial) and implicitly accounts for the effects of refraction. It allowed for self-consistent comparisons between Thomson-scattering measurements and hydrodynamic simulations by comparing the inferred values from the measurement to the intensity-weighted average value in the calculated interaction volume.

An alternative approach to calculating plasma gradients that avoids relying on hydrodynamic predictions is to calcu-

late the gradients iteratively using the measured spectra. This technique relies on the fact that the density and flow velocity can be determined relatively accurately without knowledge of the gradients. The temporal derivatives of the density and fluid velocity can be determined using time-resolved spectra, and the spatial derivatives can be calculated using conservation of mass and momentum. Assuming that the Thomson-scattering volume is small compared to the relevant scale lengths, the electron density and fluid velocity and their spatial and temporal derivatives can be treated as 1-D constants (spatially) over the scattering volume. The continuity and momentum equations for species α are

$$\frac{\partial n_\alpha}{\partial t} + \frac{\partial}{\partial x} n_\alpha u_\alpha = 0,$$

$$\frac{\partial u_\alpha}{\partial t} + u_\alpha \frac{\partial u_\alpha}{\partial x} = -\frac{1}{m_\alpha n_\alpha} \frac{\partial}{\partial x} n_\alpha T_\alpha.$$

Defining the mass density ($\rho \equiv \sum_\alpha m_\alpha n_\alpha$) and center-of-mass velocity ($u \equiv \rho^{-1} \sum_\alpha m_\alpha n_\alpha u_\alpha$), assuming $m_e \ll m_i$, and solving for the spatial derivatives give

$$\frac{\partial \rho}{\partial x} = \frac{\rho}{u^2 - \eta} \left(\frac{\partial u}{\partial t} - \frac{u}{\rho} \frac{\partial \rho}{\partial t} + \frac{\partial \eta}{\partial x} \right), \quad (8)$$

$$\frac{\partial u}{\partial x} = \frac{u}{u^2 - \eta} \left(\frac{\eta}{\rho u} \frac{\partial \rho}{\partial t} - \frac{\partial u}{\partial t} + \frac{\partial \eta}{\partial x} \right), \quad (9)$$

where $\eta \equiv (ZT_e + T_i)/m_i$ for a single ion species and $\eta \equiv [(Z_1 R + Z_2)T_e + (1+R)T_i]/(m_1 R + m_2)$ for two-ion species ($R \equiv n_1/n_2$). These equations are unchanged if the mass density is replaced by the electron density because the constant factor of $\rho = n_e(m_1 R + m_2)/(Z_1 R + Z_2)$ cancels out. Equations (8) and (9) do not allow for an iterative calculation of the terms involving the spatial gradients in temperature, but these are usually negligible.

2. Instrument Effects

Variations in the probed wave vector (because of the finite f number of the probe and collection optics) can lead to asymmetry in both the amplitude and width of the two IAW peaks. A wave-vector gradient results in asymmetric IAW peaks when variations in the probed wave vector result in the two scattering peaks being shifted by different magnitudes. The source of this asymmetry is the fact that the term corresponding to the propagation of IAW's in Eq. (5) (the first term on the right-

hand side) causes the red- and blue-shifted IAW peaks to shift in opposite directions when the magnitude of the probed wave vector is varied, but the Doppler-shifted term (last term on the right-hand side) shifts both peaks in the same direction. A sufficient condition for wave-vector gradients to cause asymmetry in an IAW spectrum is

$$\left| \frac{\partial \Delta \omega_+}{\partial k} \right| - \left| \frac{\partial \Delta \omega_-}{\partial k} \right| = |c_s - u \cos \theta_f| - |c_s + u \cos \theta_f| \neq 0, \quad (10)$$

where θ_f is the angle between the flow velocity and the probed wave vector (\mathbf{k}). This inequality is satisfied whenever $c_s > 0$, $u > 0$, and $\cos \theta_f \neq 0$. This correction has a significant impact when using the IAW feature to infer the relative drift between the ions and electrons.²³

The range of probed wave vectors was determined by treating the focusing and collection optics as a superposition of point sources and calculating each pairwise interaction. The wave-vector gradients cannot be approximated by 1-D Gaussian distributions because variations in the probed wave vector affect the magnitude of the observed wave vector and

its projection along the fluid velocity. Each pairwise interaction was sorted into a bivariate histogram of wave-vector magnitude and projection along the fluid velocity (100 bins were used).

Figure 147.20 shows spectra calculated with and without gradient/wave-vector effects. To show the amount of broadening introduced by the gradients, the “no-gradients” spectra in Fig. 147.20 correspond to the same plasma parameters as the spectra where gradients were included. The IAW spectra [Fig. 147.20(a)], including the effects of gradients results in a nearly constant amount of spectral broadening because probed wave-vector gradients (which do not vary in time), were the dominant source of broadening. Density gradients cause significant broadening of the EPW spectral peaks [Fig. 147.20(b)] only during the rise of the laser pulse and after the laser is turned off because the temporal gradients vanish and the density scale length is relatively long when the plasma is in steady state.

Error

Figure 147.21 shows the electron densities and temperatures inferred from the EPW spectra and the plasma temperatures inferred from the IAW spectra. The plasma parameters predicted by 1-D hydrodynamic simulations (*LILAC*) are shown

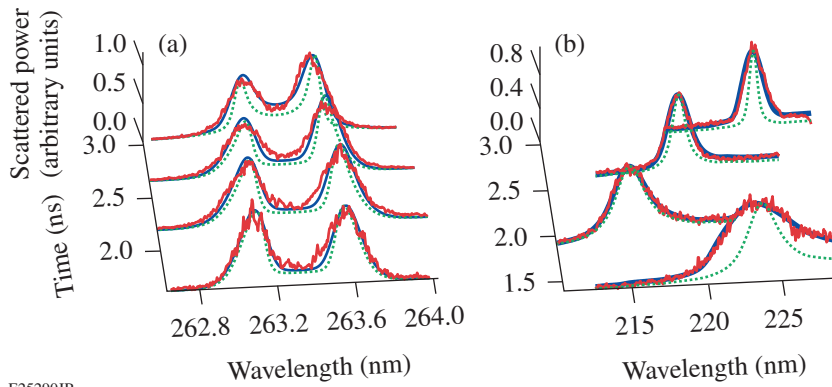


Figure 147.20 Measured spectral lineouts (red) and the corresponding calculated spectra (blue) at several different times for the (a) IAW and (b) EPW collected at 400 μm from the initial target surface. The green dotted curves correspond to calculated spectra using the same plasma parameters as the best-fit curve (blue) but without including gradient/wave-vector effects.

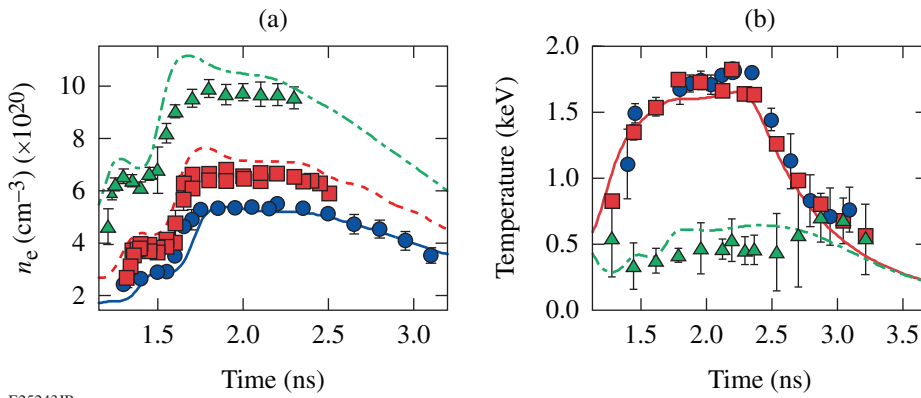


Figure 147.21 (a) Measured (symbols) and simulated (curves) electron density at 400 μm (circles), 300 μm (squares), and 200 μm (triangles) from the initial target surface. (b) Electron temperature inferred from IAW (squares) and EPW (circles) spectra, and ion temperature (triangles) inferred from the IAW spectra at 400 μm. The error in absolute timing is ~100 ps.

as solid curves. Because the error in Thomson-scattering measurements is sensitive to a number of fixed parameters, a Monte Carlo approach was used for the analysis. The inferred plasma parameters and error bars shown in Fig. 147.21 correspond to the mean and standard deviation of 100 fits, where the fixed parameters shown in Table 147.III were varied on each iteration using normally distributed values with variances characteristic to each parameter. The uncertainties shown in Table 147.III are generous estimates because the actual uncertainties (particularly in the gradients, which were the dominant source of error) are not well characterized. The error introduced by noise was accounted for by adding random noise (on each iteration) with variance equal to the variance between the measured spectrum and the initial best fit.

Table 147.III: Uncertainties included in error analysis.

Parameter	Standard deviation
Point-spread function	20%
Spectrometer dispersion	2%
Spectrometer alignment	100 μm
Gradients	20%

Summary

Simultaneous measurements of IAW and EPW Thomson-scattering spectra were obtained using a 263.25-nm probe beam. A fully reflective collection system was used to record light scattered from EPW's at electron densities up to 10^{21} cm^{-3} , which produced scattering peaks near 200 nm. An accurate analysis of the experimental Thomson-scattering spectra required accounting for plasma gradients, instrument sensitivity, optical effects, and background radiation. Two methods for calculating plasma gradients using hydrodynamic simulations or by fitting measured spectra iteratively were presented. Fits to measured Thomson-scattering spectra show the importance of including gradient effects. For example, the electron temperature inferred from the EPW feature was overestimated by ~35% when density gradients were neglected. The ion temperature was overestimated by ~50% when gradients in the flow and finite optical effects were neglected. The finite diameter of the probe focusing and collection optics was shown to introduce an asymmetry in the amplitude and width of the IAW features when a plasma flow was present.

ACKNOWLEDGMENT

This material is based upon work supported by the Department of Energy National Nuclear Security Administration under Award Number DE-NA0001944, the University of Rochester, and the New York State Energy Research and Development Authority.

REFERENCES

1. D. H. Froula, S. H. Glenzer, N. C. Luhmann, and J. Sheffield, *Plasma Scattering of Electromagnetic Radiation: Theory and Measurement Techniques*, 2nd ed. (Academic Press, Burlington, MA, 2011).
2. J. Katz, R. Boni, C. Sorce, R. Follett, M. J. Shoup III, and D. H. Froula, *Rev. Sci. Instrum.* **83**, 10E349 (2012).
3. S. H. Glenzer *et al.*, *Phys. Rev. Lett.* **82**, 97 (1999).
4. D. S. Montgomery *et al.*, *Phys. Rev. Lett.* **87**, 155001 (2001).
5. D. H. Froula, L. Divol, H. A. Baldis, R. L. Berger, D. G. Braun, B. I. Cohen, R. P. Johnson, D. S. Montgomery, E. A. Williams, and S. H. Glenzer, *Phys. Plasmas* **9**, 4709 (2002).
6. C. E. Clayton, C. Joshi, and F. F. Chen, *Phys. Rev. Lett.* **51**, 1656 (1983).
7. S. H. Glenzer *et al.*, *Phys. Rev. Lett.* **86**, 2565 (2001).
8. D. H. Froula, L. Divol, and S. H. Glenzer, *Phys. Rev. Lett.* **88**, 105003 (2002).
9. K. L. Baker, R. P. Drake, B. S. Bauer, K. G. Estabrook, A. M. Rubenchik, C. Labaune, H. A. Baldis, N. Renard, S. D. Baton, E. Schifano, A. Michard, W. Seka, and R. E. Bahr, *Phys. Rev. Lett.* **77**, 67 (1996).
10. C. Niemann, R. L. Berger, L. Divol, D. H. Froula, O. Jones, R. K. Kirkwood, N. Meezan, J. D. Moody, J. S. Ross, C. Sorce, L. J. Suter, and S. H. Glenzer, *Phys. Rev. Lett.* **100**, 045002 (2008).
11. H. A. Baldis and C. J. Walsh, *Phys. Fluids* **26**, 1364 (1983).
12. R. K. Follett, D. H. Edgell, R. J. Henchen, S. X. Hu, J. Katz, D. T. Michel, J. F. Myatt, J. Shaw, and D. H. Froula, *Phys. Rev. E* **91**, 031104(R) (2015).
13. J. F. Myatt, W. Rozmus, V. Yu. Bychenkov, and V. T. Tikhonchuk, *Phys. Rev. E* **57**, 3383 (1998).
14. J. Zheng, C. X. Yu, and Z. J. Zheng, *Phys. Plasmas* **4**, 2736 (1997).
15. J. Zheng, C. X. Yu, and Z. J. Zheng, *Phys. Plasmas* **6**, 435 (1999).
16. T. E. Tierney IV *et al.*, *J. Phys. A, Math. Gen.* **36**, 5981 (2003).
17. D. R. Nicholson, *Introduction to Plasma Theory, Wiley Series in Plasma Physics* (Wiley, New York, 1983).

18. V. N. Goncharov, T. C. Sangster, R. Betti, T. R. Boehly, M. J. Bonino, T. J. B. Collins, R. S. Craxton, J. A. Delettrez, D. H. Edgell, R. Epstein, R. K. Follet, C. J. Forrest, D. H. Froula, V. Yu. Glebov, D. R. Harding, R. J. Henchen, S. X. Hu, I. V. Igumenshchev, R. Janezic, J. H. Kelly, T. J. Kessler, T. Z. Kosc, S. J. Loucks, J. A. Marozas, F. J. Marshall, A. V. Maximov, R. L. McCrory, P. W. McKenty, D. D. Meyerhofer, D. T. Michel, J. F. Myatt, R. Nora, P. B. Radha, S. P. Regan, W. Seka, W. T. Shmayda, R. W. Short, A. Shvydky, S. Skupsky, C. Stoeckl, B. Yaakobi, J. A. Frenje, M. Gatu-Johnson, R. D. Petrasso, and D. T. Casey, *Phys. Plasmas* **21**, 056315 (2014).
19. T. R. Boehly, R. S. Craxton, T. H. Hinterman, J. H. Kelly, T. J. Kessler, S. A. Kumpan, S. A. Letzring, R. L. McCrory, S. F. B. Morse, W. Seka, S. Skupsky, J. M. Soures, and C. P. Verdon, *Rev. Sci. Instrum.* **66**, 508 (1995).
20. A. J. Mackinnon, S. Shiromizu, G. Antonini, J. Auerbach, K. Haney, D. H. Froula, J. Moody, G. Gregori, C. Constantin, C. Sorce, L. Divol, R. L. Griffith, S. Glenzer, J. Satariano, P. K. Whitman, S. N. Locke, E. L. Miller, R. Huff, K. Thorp, W. Armstrong, W. Bahr, W. Seka, G. Pien, J. Mathers, S. Morse, S. Loucks, and S. Stagnitto, *Rev. Sci. Instrum.* **75**, 3906 (2004).
21. T. J. Kessler, Y. Lin, J. J. Armstrong, and B. Velazquez, *Proc. SPIE* **1870**, 95 (1993).
22. J. Delettrez, R. Epstein, M. C. Richardson, P. A. Jaanimagi, and B. L. Henke, *Phys. Rev. A* **36**, 3926 (1987).
23. J. Hawreliak *et al.*, *J. Phys. B: At. Mol. Opt. Phys.* **37**, 1541 (2004).